The Flow in Surf Zone Waves

by

J. Veeramony and I. A. Svendsen

RESEARCH REPORT NO. CACR-99-08
December, 1999

Center for Applied Coastal Research
Ocean Engineering Laboratory
University of Delaware
Newark, DE 19716

The Flow in Surf Zone Waves

J. Veeramony[1] and I.A. Svendsen [2]

Abstract

An extended set of Boussinesq equations, which is used to model breaking waves, is derived. The wave breaking is described by accounting for the effect of vorticity generated by the breaking process. The vorticity field in the domain is obtained by solving the vorticity transport, which is based on the Reynold's equations. The boundary conditions to solve for the vorticity are obtained from measurements in hydraulic jumps. In addition to predicting the wave height decay and profile deformation, the present model also provides information about the velocity field. Comparisons with laboratory measurements show that the model results give good agreement with experimental data for wave height, setup and the velocity profiles. The undertow profiles predicted by the model are also in good agreement with the results from experimental data. The cross-shore variation of the radiation stress calculated from the model results gives a good representation of the results from experimental data.

KEYWORDS: Surf zone, Breaking waves, Vorticity, Boussinesq models

1. Introduction

Wave breaking is a natural phenomenon that is widespread in the nearshore region. By this process, energy is transferred from the organized wave motion to both high frequency turbulence and to low frequency motion such as infragravity waves, longshore/cross-shore currents and shear waves. These low frequency motions are not

[1]Post-Doctoral Fellow, Center for Ocean and Atmospheric Modeling, Building 1103, Room 249, Stennis Space Center, MS 39529, USA. **Email**: veeramon@glacier.nrlssc.navy.mil

[2]Professor, Center for Applied Coastal Research, University of Delaware, Newark, DE 19716, USA. **Email**: ias@coastal.udel.edu

always visible to the naked eye, yet they play a very important role in the surf-zone dynamics. Breaking waves are also the primary agents in sediment motions on a coast. To model all these processes accurately, the breaking process and the velocity field it creates in the surf zone have to be modelled accurately.

Recently, CFD simulations of breaking waves have been performed by Lin and Liu (1998a, 1998b). They solved the Reynolds equations for the mean flow and the $k-\epsilon$ equation for turbulent kinetic energy using the VOF method. The model results and experimental data were found to be in good agreement. The advantage of this type of modelling is that the flow details such as the turbulent intensities and the shear stresses can be directly evaluated from the model results. However, it takes about 48 hours of CPU time on a supercomputer to simulate one minute of real time for the two-dimensional case. Consequently, applications to practical cases are limited.

Hence, modelling of breaking waves using shallow water theories such as the non-linear shallow water equations or the Boussinesq equations remain of practical importance. In the past few years, Boussinesq models have been used very extensively to model waves in the nearshore region. The classical Boussinesq model (see e.g. Boussinesq 1872; Mei and LeMehaute 1966; Peregrine 1967) is a weakly non-linear, weakly dispersive wave model, which represents shallow water waves of moderate amplitude quite well.

A substantial amount of effort has gone into extending the validity of the classical equations to intermediate and deep water regimes by improving either the linear dispersion characteristics of the weakly dispersive model (e.g. Madsen *et al.* 1991; Nwogu 1993), or by including higher order dispersive terms (Madsen and Schäffer 1998a; Gobbi *et al.* 1999). Similarly, the shoaling characteristics have been improved by including full non-linear effects up to the order of dispersion retained (e.g. Wei *et al.* 1995; Madsen *et al.* 1996).

On the other hand, incorporation of wave breaking in such models has followed heuristic principles. The classical Boussinesq models conserve energy. To extend such

models to predict the wave motion in the surf zone, it is necessary to determine the way in which breaking and the associated energy dissipation change those equations.

The signature of the breaking can be included in Boussinesq models in several ways. One method is based on the concept of an artificial eddy viscosity term of the form $(\nu_t u_x)_x$, which is added to the momentum equations (Zelt 1991; Karambas and Koutitas 1992; Wei *et al.* 1995). This term essentially has the same form as the turbulent normal stresses in the horizontal direction. The value of the eddy viscosity is calibrated with experimental data. With suitable choices for the eddy viscosity, very good approximations to the wave height data can be obtained. However, there is no physical justification for such a viscosity term. It is also a disadvantage that the velocity profile remains unchanged from the standard quadratic profile (or a higher order polynomial depending upon the order of the terms retained in the Boussinesq theory) because the flow is still modelled as a potential flow.

Other methods use the concept of a surface roller first used by Svendsen (1984a, 1984b). Brocchini *et al.* (1991) used the concept introduced by Deigaard and Fredsoe (1989), where the breaking term is incorporated in the model as an additional pressure term due to the weight of the roller. In the breaking model proposed by Schäffer *et al.* (1993), the roller rides on the front face of the wave at the speed of the wave. The velocity is assumed to have a constant value in the roller region equal to about 1.3 times the wave speed. This introduces a change in the velocity profile once the waves break, and hence an excess momentum flux, which simulates wave breaking. As before, comparisons with experimental data show that the results for the wave heights and setup can be modelled quite accurately although the flow is essentially modelled as a potential flow. However, physically, the velocity profile assumed in such models is unrealistic. In addition, the roller is modelled as a solid body that travels with the wave. Lin and Rockwell (1994) showed experimentally that this is not the case.

In reality, the presence of particle velocities in the roller in excess of the phase speed and the turbulence generated are closely associated with the strong vorticity

produced by the breaking process. This is used in the breaking description in the third approach (Svendsen *et al.* 1996). The vertical distribution of the vorticity is obtained by solving the transport equation for vorticity. That is also the approach used in the present paper, and the work described is a further development of the first version of the method.

The paper is organized as follows. In section 2, the basic governing equations are derived from the depth-averaged continuity and momentum equations. The vorticity transport equation for the turbulent flow is derived in section 3. Section 4 describes the boundary conditions for the vorticity obtained from measurements in hydraulic jumps. Section 5 presents the evaluation of the breaking terms, and in section 6 we derive the procedure for wave generation at the seaward boundary which also includes a generating-absorbing boundary condition. Section 7 shows comparisons between experimental data and computed results for wave properties such as surface elevation, wave heights, velocity field, and undertow. The wave radiation stress is also discussed. Section 8 presents the conclusions.

2. The basic equations.

2.1 *Length scales and non-dimensionalization.*

The two independent non-dimensional parameters which characterize shallow water waves are the relative wave height $\delta = a_0/h_0$ and the relative wave length $\mu = k_0 h_0$. Here, a_0, h_0 and k_0 represent the characteristic wave amplitude, water depth and wave number respectively. In this study, we restrict ourselves to shallow water waves, $\mu^2 \ll O(1)$. Furthermore, as a first approximation, we also restrict analysis to the weakly non-linear case, $\delta < O(1)$. Thus, all terms $O(\delta\mu^2)$ and smaller are neglected. As will be seen later, this assumption of weak non-linearity represents the largest source of inaccuracies close to the breaking region (see e.g. Wei *et al.* 1995; Madsen *et al.* 1997a).

For shallow water waves, the independent variables are scaled as

$$x = k_0\hat{x}, \qquad z = \hat{z}/h_0, \qquad \text{and} \qquad t = k_0\sqrt{gh_0}\hat{t}, \tag{1}$$

where the $\hat{()}$ represents the dimensional quantities. The dependent variables $\hat{\zeta}$ (water surface elevation) and $\hat{\psi}$ (streamfunction) are scaled as

$$\zeta = \hat{\zeta}/a_0, \qquad \psi = \hat{\psi}/(\delta h_0 \sqrt{g h_0}). \tag{2}$$

Using these scales, the non-dimensional horizontal velocity (u), the vertical velocity (w) and the vorticity (ω) are

$$\hat{u} = \frac{\partial \psi}{\partial z} = \delta \sqrt{g h_0}\, u, \tag{3}$$

$$\hat{w} = -\frac{\partial \psi}{\partial x} = \delta \mu \sqrt{g h_0}\, w, \tag{4}$$

$$\hat{\omega} = \frac{\partial \hat{u}}{\partial \hat{z}} - \frac{\partial \hat{w}}{\partial \hat{x}} = \frac{\delta \sqrt{g h_0}}{h_0} \left(\frac{\partial u}{\partial z} - \mu^2 \frac{\partial w}{\partial x} \right) = \frac{\delta \sqrt{g h_0}}{h_0}\, \omega. \tag{5}$$

For irrotational motion where $\omega = 0$, $\partial u/\partial z = \partial w/\partial x$. In that case, to the lowest order of approximation, u does not vary over depth. In the case of breaking waves, however, the vorticity is quite strong, which implies that $\partial u/\partial z \sim O(1)$. To develop a model that describes breaking waves in the nearshore region, we start with the depth-integrated equations of continuity and momentum.

2.2 *Depth integrated continuity and momentum equations.*

The depth-integrated continuity equation is

$$\frac{\partial \zeta}{\partial t} + \frac{\partial Q}{\partial x} = 0, \tag{6}$$

where the volume flux Q is

$$Q \equiv \int_{-h}^{\delta \zeta} u \, dz. \tag{7}$$

In this study, only the region from intermediate/shallow water depths to the shoreline is considered. Then, the effect of horizontal surface forces, such as due to wind, is minimal since the fetch area is very small. To further simplify the problem, we choose at this time to neglect the shear stresses at the bottom. This, in essence, implies a free-slip condition at the sea bed. The depth-integrated horizontal momentum equation is (see e.g. Mei 1992)

$$\frac{\partial Q}{\partial t} + \delta \frac{\partial}{\partial x} \int_{-h}^{\delta \zeta} u^2 \, dz = p(-h) \frac{\partial h}{\partial x} - \frac{\partial}{\partial x} \int_{-h}^{\delta \zeta} p \, dz, \tag{8}$$

and, the depth-integrated vertical momentum equation is (see e.g. Mei 1992)

$$p(z) = (\zeta - \frac{z}{\delta}) - \delta\mu^2 w^2 + \mu^2 \frac{\partial}{\partial t} \int_z^{\delta\zeta} w \, dz + \delta\mu^2 \frac{\partial}{\partial x} \int_z^{\delta\zeta} uw \, dz. \tag{9}$$

Using (9) to eliminate the pressure p from (8), and replacing the vertical velocity by the horizontal velocity using the continuity equation, (8) becomes

$$\begin{aligned} \frac{\partial Q}{\partial t} + \delta \frac{\partial}{\partial x} \int_{-h}^{\delta\zeta} u^2 \, dz + (h + \delta\zeta)\zeta_x - \mu^2 \int_{-h}^{\delta\zeta} \frac{\partial^2}{\partial x \partial t} \int_z^{\delta\zeta} \frac{\partial}{\partial x} \int_{-h}^{z} u \, dz \, dz \, dz \\ - \delta\mu^2 \int_{-h}^{\delta\zeta} \frac{\partial}{\partial x} \left(\frac{\partial}{\partial x} \int_{-h}^{z} u \, dz \right)^2 dz \\ - \delta\mu^2 \int_{-h}^{\delta\zeta} \frac{\partial^2}{\partial x^2} \int_z^{\delta\zeta} u \frac{\partial}{\partial x} \int_{-h}^{z} u \, dz \, dz \, dz = 0. \end{aligned} \tag{10}$$

2.3 *Equation for horizontal velocity.*

To solve (6) and (10), the depth variation of the horizontal velocity u must be determined. In the classical derivation of Boussinesq models, the shallow water assumption is utilized to represent the vertical variation of the velocity potential (ϕ) by an infinite polynomial series. The coefficients of this polynomial are obtained by solving the Laplacian and applying the boundary condition on ϕ. From this approximation of ϕ, the depth variation of u is obtained. However, in the surf-zone, the velocities can no longer be represented by a potential function because of the vorticity generated by the breaking waves. Instead, we use the streamfunction ψ, which satisfies

$$\mu^2 \psi_{xx} + \psi_{zz} = \omega, \tag{11}$$

with the boundary conditions

$$\psi(z = -h) = 0, \tag{12a}$$

$$\psi_z(z = -h) = u_0. \tag{12b}$$

Integrating (11) twice, from the bottom to an arbitrary location z in the water column, gives

$$\psi = -\int_{-h}^{z} \int_{-h}^{z} \mu^2 \psi_{xx} \, dz \, dz + \int_{-h}^{z} \int_{-h}^{z} \omega \, dz \, dz + u_0(z + h). \tag{13}$$

To the lowest order in μ^2, we have

$$\psi = \int_{-h}^{z}\int_{-h}^{z} \omega \, dz \, dz + u_0(z+h), \tag{14}$$

which gives

$$\psi_{xx} = \int_{-h}^{z}\int_{-h}^{z} \omega_{xx} \, dz \, dz + u_{0_{xx}}(z+h) + u_0 h_{xx} + 2u_{0_x}h_x, \tag{15}$$

where we have used free slip condition at the bottom. Substituting (15) into (13) gives the expression for ψ

$$\begin{aligned}\psi =& u_0(z+h) - \frac{1}{6}\mu^2 u_{0_{xx}}(z+h)^3 + \int_{-h}^{z}\int_{-h}^{z} \omega \, dz \, dz \\ &- \frac{1}{2}\mu^2(z+h)^2\left(u_0 h_{xx} + 2u_{0_x}h_x\right) - \mu^2 \int_{-h}^{z}\int_{-h}^{z}\int_{-h}^{z}\int_{-h}^{z} \omega_{xx} \, dz \, dz \, dz \, dz. \end{aligned} \tag{16}$$

From (16), the horizontal velocity is obtained by differentiation with respect to z as

$$\begin{aligned} u = u_0 - \mu^2(z+h)[2h_x u_{0_x} + h_{xx}u_0] - \frac{\mu^2}{2}u_{0_{xx}}(z+h)^2 \\ + \int_{-h}^{z} \omega \, dz - \mu^2 \int_{-h}^{z}\int_{-h}^{z}\int_{-h}^{z} \omega_{xx} \, dz \, dz \, dz + O(\mu^4). \end{aligned} \tag{17}$$

Notice that there are two basic components in the expression for the horizontal velocity. The first three terms constitute the expression for the horizontal velocity in the classical weakly nonlinear, weakly dispersive Boussinesq equations (Peregrine 1967). The rest of the terms are associated with the presence of vorticity in the flow field. Thus, we define the potential component of the velocity (u_p) and the rotational component of the velocity (u_r) as

$$u_p \equiv u_0 - \mu^2(z+h)[2h_x u_{0_x} + h_{xx}u_0] - \frac{\mu^2}{2}u_{0_{xx}}(z+h)^2 + O(\mu^4), \tag{18a}$$

$$u_r \equiv \int_{-h}^{z} \omega \, dz - \mu^2 \int_{-h}^{z}\int_{-h}^{z}\int_{-h}^{z} \omega_{xx} \, dz \, dz \, dz + O(\mu^4), \tag{18b}$$

so that

$$u = u_p + u_r. \tag{19}$$

The potential part of the velocity is now expressed in terms of the depth averaged potential velocity U_p as (see e.g. Dingemans 1997)

$$u_p = U_p - \mu^2(\frac{h}{2} + z)(hU_p)_{xx} + \frac{\mu^2}{2}\left(\frac{h^2}{3} - z^2\right)U_{p_{xx}} + O(\delta\mu^2, \mu^4). \tag{20}$$

where

$$U_p \equiv \frac{1}{h + \delta\zeta}\int_{-h}^{\delta\zeta} u_p \, dz \tag{21}$$

2.4 *The weakly nonlinear breaking model.*

From (10), keeping terms only larger than $O(\delta\mu^2, \mu^4)$, we have

$$\frac{\partial Q}{\partial t} + \delta\frac{\partial}{\partial x}\int_{-h}^{\delta\zeta} u^2 \, dz + (h + \delta\zeta)\zeta_x + \mu^2\int_{-h}^{\delta\zeta}\frac{\partial^2}{\partial x \partial t}\int_z^{\delta\zeta}\frac{\partial}{\partial x}\int_{-h}^{z} u \, dz \, dz \, dz = 0. \tag{22}$$

We now have, using the results from the previous section,

$$\begin{aligned}
\int_{-h}^{\delta\zeta} u^2 \, dz &= \int_{-h}^{\delta\zeta}(U_p + u_r)^2 \, dz + O(\mu^2) \\
&= \int_{-h}^{\delta\zeta}({U_p}^2 + 2U_pU_r + {U_r}^2) + (2U_pu_r + u_r^2 - 2U_pU_r - {U_r}^2) \, dz + O(\mu^2) \\
&= (h + \delta\zeta)U^2 + \int_{-h}^{\delta\zeta}(u_r^2 - {U_r}^2) \, dz + O(\mu^2) \\
&= \frac{Q^2}{h + \delta\zeta} + \Delta M + O(\mu^2),
\end{aligned} \tag{23}$$

where U is the total depth averaged velocity, Q the total volume flux including the contribution from the depth-averaged component of the rotational part of the velocity and

$$\Delta M \equiv \int_{-h}^{\delta\zeta}(u_r^2 - {U_r}^2) \, dz. \tag{24}$$

Similarly,

$$\begin{aligned}
\int_{-h}^{\delta\zeta}\frac{\partial^2}{\partial x \partial t}\int_z^{\delta\zeta}\frac{\partial}{\partial x}\int_{-h}^{z} u \, dz \, dz \, dz &= \int_{-h}^{\delta\zeta}\frac{\partial^2}{\partial x \partial t}\int_z^{\delta\zeta}\frac{\partial}{\partial x}\int_{-h}^{z}(U_p + u_r) \, dz \, dz \, dz + O(\mu^2) \\
&= \frac{h^2}{2}Q_{xxt} - \frac{h^3}{6}\left(\frac{Q}{h}\right)_{xxt} - (\Delta P)_{xxt} + O(\delta, \mu^2),
\end{aligned} \tag{25}$$

where

$$\Delta P \equiv \int_{-h}^{\delta\zeta} \int_{z}^{\delta\zeta} \int_{-h}^{z} (u_r - U_r)\, dz\, dz\, dz. \tag{26}$$

Substituting (23) and (25) into (22) gives

$$\frac{\partial Q}{\partial t} + (h+\delta\zeta)\frac{\partial \zeta}{\partial x} + \delta\left(\frac{Q^2}{h+\delta\zeta}\right)_x - \mu^2 \frac{h^2}{2} Q_{xxt} + \mu^2 \frac{h^3}{6}\left(\frac{Q}{h}\right)_{xxt} + \delta\left(\Delta M\right)_x + \mu^2\left(\Delta P\right)_{xxt} = 0. \tag{27}$$

Equations (6) and (27) form the basis of the breaking model. However, the dispersion characteristics of the model are very poor for intermediate and deep water waves. Madsen and Schäffer (1998b) suggests enhancement of the frequency dispersion by applying a linear operator

$$L = 1 + B\mu^2 h^2 \frac{\partial^2}{\partial x^2} \tag{28}$$

on (27) and retaining terms of $O(\delta, \mu^2)$. Here, B is a free parameter, chosen such that the dispersion characteristic most closely resemble that of fully dispersive linear theory. Thus, (27) becomes

$$\frac{\partial Q}{\partial t} + (h+\delta\zeta)\frac{\partial \zeta}{\partial x} + \delta\left(\frac{Q^2}{h+\delta\zeta}\right)_x + \mu^2\left(B - \frac{1}{2}\right) h^2 \left(Q\right)_{xxt} + \mu^2 \frac{h^3}{6}\left(\frac{Q}{h}\right)_{xxt} + Bgh^2(h\zeta_x)_{xx} + \delta\left(\Delta M\right)_x + \mu^2\left(\Delta P\right)_{xxt} = 0. \tag{29}$$

Madsen *et al.* (1991) found that $B = -1/15$ gives the closest approximation to linear dispersion and is therefore the value used in the following. The last two terms in (29) depend entirely on the vorticity field in the domain. Thus, in the shoaling region where there is no generation of vorticity, these terms vanish, and (29) reduces to the classical Boussinesq equations with dispersion correction. On the other hand, inside the surf-zone the vorticity terms are the only signatures of breaking, as vorticity is generated due to the breaking process leading to non-zero contributions from ΔM and ΔP.

Equations (6) and (29) together constitute the equations for conservation of mass and momentum for the breaking waves. Thus, there are two equations and

three unknowns (ζ, Q and ω), which means that an additional equation is necessary to close the problem. This is achieved by using the vorticity transport equation to determine the vorticity distribution in the breaking waves.

3. The 2-D vorticity transport equation.

The vorticity transport equation for the turbulent flow can be derived from the Reynolds equations, which in two dimensions are

$$\frac{\partial \widetilde{\hat{u}}}{\partial \hat{t}} + \widetilde{\hat{u}}\frac{\partial \widetilde{\hat{u}}}{\partial \hat{x}} + \widetilde{\hat{w}}\frac{\partial \widetilde{\hat{u}}}{\partial \hat{z}} = -\frac{1}{\rho}\frac{\partial \widetilde{\hat{p}}}{\partial \hat{x}} + \frac{1}{\rho}\left(\frac{\partial \hat{\tau}_{xx}}{\partial \hat{x}} + \frac{\partial \hat{\tau}_{zx}}{\partial \hat{z}}\right), \tag{30a}$$

$$\frac{\partial \widetilde{\hat{w}}}{\partial \hat{t}} + \widetilde{\hat{u}}\frac{\partial \widetilde{\hat{w}}}{\partial \hat{x}} + \widetilde{\hat{w}}\frac{\partial \widetilde{\hat{w}}}{\partial \hat{z}} = -\frac{1}{\rho}\frac{\partial \widetilde{\hat{p}}}{\partial \hat{z}} + \frac{1}{\rho}\left(\frac{\partial \hat{\tau}_{xz}}{\partial \hat{x}} + \frac{\partial \hat{\tau}_{zz}}{\partial \hat{z}}\right), \tag{30b}$$

where the $\widetilde{()}$ indicates ensemble averaged quantities and $\hat{\tau}_{xz}$ and $\hat{\tau}_{zz}$ are the Reynolds stresses based on the ensemble averaged velocities. The pressure is eliminated from equations (30a) and (30b) to give

$$\frac{\partial \widetilde{\hat{\omega}}}{\partial \hat{t}} + \widetilde{\hat{u}}\frac{\partial \widetilde{\hat{\omega}}}{\partial \hat{x}} + \widetilde{\hat{w}}\frac{\partial \widetilde{\hat{\omega}}}{\partial \hat{z}} = \frac{1}{\rho}\left[\frac{\partial^2}{\partial \hat{x}\partial \hat{z}}\left(\hat{\tau}_{xx} - \hat{\tau}_{zz}\right) - \left(\frac{\partial^2}{\partial \hat{x}^2} - \frac{\partial^2}{\partial \hat{z}^2}\right)\hat{\tau}_{zx}\right]. \tag{31}$$

If we express the Reynolds stresses in terms of an eddy viscosity $\hat{\nu}_t$, then

$$\hat{\tau}_{xx} = \rho\left[2\hat{\nu}_t\frac{\partial \widetilde{\hat{u}}}{\partial \hat{x}} - \frac{2}{3}k\right] \quad \text{and} \quad \hat{\tau}_{xz} = \rho\hat{\nu}_t\left(\frac{\partial \widetilde{\hat{u}}}{\partial \hat{z}} + \frac{\partial \widetilde{\hat{w}}}{\partial \hat{x}}\right) \tag{32}$$

where k is the turbulent kinetic energy. Assuming the eddy viscosity $\hat{\nu}_t$ to be a constant, (31) reduces to

$$\frac{\partial \widetilde{\hat{\omega}}}{\partial \hat{t}} + \widetilde{\hat{u}}\frac{\partial \widetilde{\hat{\omega}}}{\partial \hat{x}} + \widetilde{\hat{w}}\frac{\partial \widetilde{\hat{\omega}}}{\partial \hat{z}} = \hat{\nu}_t\left(\frac{\partial^2 \widetilde{\hat{\omega}}}{\partial \hat{x}^2} + \frac{\partial^2 \widetilde{\hat{\omega}}}{\partial \hat{z}^2}\right). \tag{33}$$

At the free surface, in the region that does not include the roller, we neglect the small vorticity due to viscous effects. In the roller region, the measurements from hydraulic jumps (see e.g. Svendsen *et al.* 1999) indicate that the free surface vorticity will also be close to zero. However, strong vorticity is generated inside the roller region. We approximate this vorticity generated by the vorticity at the

"dividing" region between the roller and the interior. Thus, the boundary conditions used for the vorticity are

$$\widetilde{\hat{\omega}}(\hat{z} = \widetilde{\hat{\zeta}}_e, \hat{t}) = \widetilde{\hat{\omega}}_s(\hat{x}, \hat{t}), \tag{34a}$$

$$\widetilde{\hat{\omega}}(\hat{z} = -\hat{h}, \hat{t}) = 0, \tag{34b}$$

$$\widetilde{\hat{\omega}}(\hat{z}, \hat{t} = 0) = 0, \tag{34c}$$

where the values of $\widetilde{\hat{\zeta}}_e$, which is the vertical location of the lower edge of the roller, and $\widetilde{\hat{\omega}}_s(x,t)$ are discussed in the next section. As mentioned, the bottom boundary condition of zero vorticity is consistent with the assumption of a free-slip condition at the bottom.

Non-dimensionalizing (33) using the scales in (1)-(5) gives,

$$\frac{\partial \omega}{\partial t} + \delta u \frac{\partial \omega}{\partial x} + \delta w \frac{\partial \omega}{\partial z} = \nu_t \left(\mu^2 \frac{\partial^2 \omega}{\partial x^2} + \frac{\partial^2 \omega}{\partial z^2} \right). \tag{35}$$

where the $\widetilde{()}$'s are omitted for convenience.

Notice that in (29), the terms involving breaking are formally $O(\delta)$ or $O(\mu^2)$. Therefore, we only need to retain terms of $O(1)$ in (35). We first change the coordinate system from (x, z, t) to (x, σ, t), where

$$\sigma = \frac{h + z}{h + \delta \zeta_e}, \tag{36}$$

which transforms the domain from $-h \leq z \leq \delta \zeta_e$ to $0 \leq \sigma \leq 1$. Then, the governing equation for the vorticity distribution reduces to

$$\frac{\partial \omega}{\partial t} = \kappa \frac{\partial^2 \omega}{\partial \sigma^2} + O(\delta, \mu^2), \tag{37}$$

where $\kappa = \nu_t / h^2$. The boundary conditions given by (34a)-(34c) reads, in the new coordinate system

$$\omega(\sigma = 1, t) = \omega_s(x, t), \tag{38a}$$

$$\omega(\sigma = 0, t) = 0, \tag{38b}$$

$$\omega(\sigma, t = 0) = 0. \tag{38c}$$

The boundary conditions are homogenized by redefining the dependent variable

$$\omega = \omega^{(1)} + \sigma\omega_s, \tag{39}$$

which transforms the system of equations to

$$\frac{\partial\omega^{(1)}}{\partial t} - \kappa\frac{\partial^2\omega^{(1)}}{\partial\sigma^2} = -\sigma\frac{\partial\omega_s}{\partial t}, \tag{40a}$$

$$\omega^{(1)}(\sigma = 1, t) = 0, \tag{40b}$$

$$\omega^{(1)}(\sigma = 0, t) = 0, \tag{40c}$$

$$\omega^{(1)}(\sigma, t = 0) = 0. \tag{40d}$$

The solution to this system of equations is obtained by first expressing the right hand side of (40a) in terms of a half-range sine expansion so that

$$-\sigma\frac{\partial\omega_s}{\partial t} = \sum_{n=1}^{\infty} F_n \sin n\pi\sigma, \tag{41}$$

which gives

$$F_n = 2\int_0^1 -\sigma\frac{\partial\omega_s}{\partial t}\sin n\pi\sigma \; d\sigma = (-1)^n\frac{2}{n\pi}\frac{\partial\omega_s}{\partial t}. \tag{42}$$

We now look for solutions to $\omega^{(1)}$ of the form

$$\omega^{(1)} = \sum_{n=1}^{\infty} G_n \sin n\pi\sigma. \tag{43}$$

Note that (43) satisfies the boundary conditions. Equations (43) and (41) are substituted into (40a), which gives

$$\sum_{n=1}^{\infty}\left[\frac{\partial G_n}{\partial t} + \kappa n^2\pi^2 G_n - F_n\right]\sin n\pi\sigma = 0, \tag{44}$$

which, to be true for all σ, implies that

$$\frac{\partial G_n}{\partial t} + \kappa n^2\pi^2 G_n - F_n = 0. \tag{45}$$

The solution to the ordinary differential equation (45), after substituting for F_n from (42), is

$$G_n(t) \equiv (-1)^n\frac{2}{n\pi}\int_0^t \frac{\partial\omega_s}{\partial\tau}e^{n^2\pi^2\kappa(\tau - t)}\, d\tau. \tag{46}$$

Thus, the expression for ω is

$$\omega = \sigma\omega_s + \sum_{n=1}^{\infty} G_n \sin n\pi\sigma, \tag{47}$$

with G_n defined as in (46). This solution can be evaluated when ω_s and ζ_e is specified.

4. Boundary conditions for vorticity.

Measurements of velocities and vorticity in the roller region for breaking waves are not yet available inside the surf-zone. However, viewed in a coordinate system that moves at the wave speed, breaking waves have flow patterns around the roller region that are very similar to those observed in hydraulic jumps. The absolute velocities and the bottom boundary layer would of course be different under this coordinate transformation but the turbulent stresses near the surface, the surface profile and especially the vorticity are similar.

Velocity measurements are available for hydraulic jumps for the range of Froude numbers $1.3 \simeq \mathcal{F} < 2$ (Svendsen *et al.* 1999; Lin and Rockwell 1994; Bakunin 1995). This range is similar to Froude numbers for breaking waves. The vorticity distribution was calculated from the velocity measurements in hydraulic jumps obtained by Bakunin (1995). The details of the analysis of the data can be found in Svendsen *et al.* (1999).

Figure 1 shows the variation of the horizontal velocity and the vorticity in the three jumps. The vorticity is concentrated in the upper region of the flow. Immediately behind the toe of the roller, the maximum vorticity is seen to occur at the lower edge of the roller. Further downstream, however, the maximum vorticity occurs below the roller. In addition, near the surface, the vorticity reduces to a very small value. This structure is very similar to that reported by Lin and Rockwell (1994). The vorticity generated inside the roller region is represented in the breaking model by specifying the vorticity at the lower edge of the roller.

For the three hydraulic jumps, with Froude numbers less than two, analyzed by Svendsen *et al.* (1999), it was found that the shape of the roller measured by its

thickness is similar for all three cases. Figure 2(a) shows that the roller thickness can be represented by the curve, obtained using a least squares fit to the data,

$$\frac{\widetilde{\hat{\zeta}}_e}{h_2\sqrt{\xi}} = 0.78e^{\hat{x}/\ell_r}\left(\frac{\hat{x}}{\ell_r} - \frac{\hat{x}^2}{\ell_r^2}\right), \tag{48}$$

where ℓ_r is the length of the roller, $\xi = h_2/h_1$ is the ratio of the downstream depth (h_2) to the upstream depth (h_1) and $\hat{x} = 0$ at the mean position of the toe of the roller.

Similarly, figure 2(b) shows the vorticity at the lower edge of the roller. Again, it was found that non-dimensional vorticity values for all three cases are very similar, and the dimensionless ω_s can be represented by

$$\frac{\widetilde{\hat{\omega}}_s h_2\xi}{U_1} = 15.75\left(1 - \frac{\hat{x}}{\ell_r}\right)$$

which is shown as the dashed line in the figure. It turns out that the sharp discontinuity at $\hat{x}/\ell_r = 0$, which can be expected based on physical considerations, causes numerical instabilities. The numerical computations are eased somewhat if this is replaced by the expression

$$\frac{\widetilde{\hat{\omega}}_s h_2\xi}{U_1} = 15.75\left(1 - e^{40\hat{x}/\ell_r}\right)\left(1 - \frac{\hat{x}}{\ell_r}\right) \tag{49}$$

which is shown as the solid line in figure 2b. This avoids the sharp discontinuity at $\hat{x}/\ell_r = 0$, at the same time preserving the shape of the vorticity function at the lower edge of the roller. The expressions of $\widetilde{\hat{\zeta}}_e$ and $\widetilde{\hat{\omega}}_s$ from (48) and (49) are used in the solution (47) to the vorticity equation.

Inside the roller, the vorticity decreases upwards from ω_s at the lower limit (the dividing streamline in a coordinate system following the wave) to near zero at the surface. The contribution from this region is of some importance for an accurate evaluation of the ΔM term though we do not have a detailed description of the flow inside the roller. Values are determined by interpolating between the surface and the roller limit as described in the next section. We notice that the potential part of the

flow in the roller is already included in the Q^2-term in (29).

5. Calculation of the breaking terms.

The vorticity field in the computational domain can be determined using (47). Reverting to dimensional variables and omitting the $\hat{()}$ for convenience, we define

$$Q_r = \int_{-h}^{\zeta_e} u_r \, dz \qquad \text{and} \qquad \Delta Q_r = \int_{\zeta_e}^{\zeta} u_r \, dz, \tag{50}$$

where ΔQ_r is essentially the rotational part of the volume flux due to the roller. Then, (24) can be written as

$$\Delta M = \int_{-h}^{\zeta_e} u_r^2 \, dz + \int_{\zeta_e}^{\zeta} u_r^2 \, dz - \frac{(Q_r + \Delta Q_r)^2}{h + \zeta}. \tag{51}$$

Using (47), we have

$$\begin{aligned} \Delta M = (h + \zeta_e)^3 \Bigg[& \frac{\omega_s^2}{20} + \frac{1}{2} \sum_{n=1}^{\infty} \frac{G_n^2}{n^2 \pi^2} + \left(\sum_{n=1}^{\infty} \frac{G_n}{n\pi} \right)^2 \\ & - \omega_s \sum_{n=1}^{\infty} \frac{G_n}{n\pi} \left(\frac{2 \cos n\pi}{n^2 \pi^2} + \frac{1}{3} \right) \Bigg] + \int_{\zeta_e}^{\zeta} u_r^2 \, dz - \frac{(Q_r + \Delta Q_r)^2}{h + \zeta}, \end{aligned} \tag{52}$$

where

$$Q_r = (h + \zeta_e)^2 \left[\frac{\omega_s}{6} + \sum_{n=1}^{\infty} \frac{G_n}{n\pi} \right], \tag{53}$$

From measurements in hydraulic jumps, it was found that the velocity in the roller region is approximated well by a cubic polynomial in z (which was also the approximation used by Madsen and Svendsen 1983). Therefore, the contribution to the vorticity from inside the roller is calculated using a cubic polynomial approximation.

In calculating the expression for ΔP, the contribution from the roller region is neglected, since ΔP is $O(\mu^2)$. This essentially corresponds to assuming hydrostatic pressure inside the roller. It gives

$$\begin{aligned} \Delta P &= \int_{-h}^{\zeta_e} \int_{z}^{\zeta_e} \int_{-h}^{\zeta_e} (u_r - U_r) \, d\sigma \, d\sigma \, d\sigma \\ &= -(h + \zeta_e)^4 \left[\frac{\omega_s}{45} - 2 \sum_{n=1}^{\infty} \frac{G_n}{n^3 \pi^3} \cos n\pi \right]. \end{aligned} \tag{54}$$

6. Numerical solution.

The governing equations (6) and (29) are solved using a fourth-order Adam-Bashforth-Moulton method. This method has been found accurate and effective for Boussinesq type equations by Wei and Kirby (1995) and gives a correct representation of the triple-derivative terms.

At the offshore boundary, solutions to the equations for permanent form waves are found and used as input. The approach represents a generalization of the third order Stokes solution presented by Madsen and Sørensen (1993). This makes it possible to generate large amplitude waves at the boundary. This is combined with an absorbing-generating boundary condition used at the offshore boundary to absorb the long waves reflected from the computational domain.

The derivation of the constant form solution and the absorbing-generating boundary condition for the Boussinesq equations is described in some detail in the appendix.

It is emphasized here that this procedure allows us to specify only the incoming volume flux Q_i at the seaward boundary. This is in analogy with how a wavemaker in a wave tank works. The values of ζ at the boundary upgraded to the next time step are determined from the continuity equation.

Close to the shoreline, a shelf with a very small but constant depth with a sponge layer and a wall is used to absorb the breaking waves. The start of wave breaking is usually defined as the position where the front face of the wave becomes vertical. In Boussinesq-type models, as the waves approach breaking, the amplitude dispersion balances the frequency dispersion. Consequently, the front face of the wave stabilizes before it becomes vertical. Thus, the point where the breaking is initiated for each wave has to be specified explicitly. In the present computations wave breaking is assumed to start when the maximum slope in front of the wave crest exceeds 20° (see Madsen *et al.* (1997a)). The transition period, during which the roller develops, lasts for 1/10-th of the wave period. Drawing on the results from the

measurements in hydraulic jumps, the fully developed roller extends from the wave crest to the location in front of the wave where the gradient is zero.

7. Comparison between model results and data.

The results from the model described in the previous sections were first compared to two sets of experiments with monochromatic waves. Wave heights and setup measurements for monochromatic waves are available from the experiments by Hansen and Svendsen (1979). Wave shape and the velocity profiles below the wave trough are available from the measurements by Cox *et al.* (1995). Both experiments were conducted in wave flumes with plane beaches. In the experiments of Cox *et al.* (1995) however, the bottom roughness was increased by gluing sand to the bottom, which increased the bottom friction. The computational domain, shown in figure 3, is similar to the experimental domain of both the above mentioned experiments.

7.1 *Wave height and set-up comparisons.*

The first set of comparisons is to the data from Hansen and Svendsen (1979). The experiments were conducted in a wave flume with a plain beach of slope 1:34.26. The water depth at the start of the slope was $h_0 = 0.36\ m$. Seven tests were conducted in all. The wave heights and set-up for each case was measured at a number of locations. In this paper, comparisons will only be shown for three cases. Table 1 presents the wave period and the wave height at the start of the slope for each of the cases.

Figure 4 shows the comparison between the model results and the data for Case 1. The wave heights in the initial part of the shoaling region is represented well. As the waves get closer to breaking, the difference between computed and measured wave height increases. At the point of wave breaking, the difference between the two is obvious. The reason for this discrepancy is that the present version of the potential part of the model is based on the lowest order weakly nonlinear theory as in Madsen *et al.* (1997a, 1997b). Though this can be improved, the emphasis of this study,

however, is the modelling of the phenomena after breaking. A short while after the breaking has been initiated in the model, it is seen that the agreement is again very good.

An important gauge of the model performance is also obtained from looking at the prediction of the set-up (figure 4b), which shows good agreement between the model results and the experimental data. This suggests that the evaluation of such terms as the radiation stresses will also be accurate.

Figures 5 and 6 show the comparisons for Case 2 and 3. Again, the model underestimates the wave height near the breaking region. On the other hand, the prediction of the set-up is consistently good. All this indicates that the flow properties in the surf-zone are being modelled with reasonable accuracy. To illustrate this further, the results from the model are compared to velocity data from breaking waves.

7.2 *Velocity and surface elevation comparisons to data.*

Velocity and surface elevation data were gathered by Cox *et al.* (1995). The experiments were conducted in a wave flume with a plain beach slope of 1:35. The wave height at the wavemaker was $H_0 = 11.5\ cm$ and the water depth at the start of the beach was $h_0 = 0.40\ m$. The wave period was $T_0 = 2.2\ s$. Measurements of velocity in the vertical were taken at six locations given in table 2.

The first measuring line was outside the breaking region, the second was close to the breaking point and the last four were inside the surf zone. Figure 7 shows the comparison between the data and the model predictions at the locations given in table 2. The abscissa in the figure is normalized by the wave period. The present version of the model incorporates only the lowest order nonlinear contributions. Hence, the computed wave surface shape (– – –) does not quite have the saw-tooth shape seen in the data (———) at the locations in the surf zone.

The comparison between the measured (•) and the predicted (–·–·–) velocity profiles are also shown in the figure 7. For the most part, the agreement between the two is excellent. An exception is near the toe of the turbulent breaker front ($t/T = 0.2$) where the model tends to predict a positive velocity whereas the data

shows negative velocities. The differences are likely to be due to the differences in the predicted and measured surface profiles.

Figure 8 shows the vorticity field in a breaking wave. The contour lines of vorticity (8a) show that the vorticity produced in the roller region is convected downward and towards the back of the wave. Also, the absolute maximum value of the vorticity in the wave occurs right after the toe of the roller has passed. Along each vertical cross-section, it is only close to the toe that the maximum of the vorticity is close to the lower edge of the roller. From approximately halfway through the roller region, the maximum of the vorticity is found below the lower limit of the roller. The maximum vorticity remains well below the surface as the vorticity decays downstream of the roller on the backside of the wave. These results are similar to that observed in the hydraulic jumps (see figure 1 and also Lin and Rockwell (1994)). Thus, the important features of the vorticity distribution are captured by the model.

7.3 *Comparison of undertow profiles.*

When starting the computations of the waves from a cold start, a significant surge is also initiated in the tank. After a while, when the surge has settled, there is a strong seaward mass flux near the bottom (the undertow), which is particularly pronounced inside the surf zone. The total horizontal velocity (u) can be separated into an oscillatory wave component (u_w) and a current component (V) which is constant over a wave period. The total mass flux over a wave period is given by

$$\overline{Q} = \overline{\int_{-h}^{\zeta} u_w + V \, dz}, \tag{55}$$

where $\overline{()}$ represents averaging over a wave period. The oscillatory or wave component is defined so that the mean velocity $\overline{u}_w$ below trough is zero. This also implies that the mass flux due to waves below the trough level is zero, and therefore

$$\overline{Q} = \overline{\int_{\zeta_t}^{\zeta} u_w \, dz} + \int_{-h}^{\bar{\zeta}} V \, dz, \tag{56}$$

where the first integral is the mass flux $\overline{Q}_w$ due to the wave motion. The undertow $V(z)$ is then the Eulerian mean of the velocity u below trough.

The model results of the undertow profiles are shown in (Figure 9) together with the results from the measurements of Cox *et al.* (1995). Outside the surf-zone ($h = 28.0\ cm$ and $h = 21.14\ cm$) the results from the model show that there is no vertical variation of the undertow. This is consistent with the fact that outside the breaking point the wave motion is irrotational. In the transition region ($h = 17.71\ cm$), model results underestimate the undertow over most of the water column, although not very significantly. On the other hand, the agreement between the model and the data is extremely good in the inner surf zone ($h = 14.29\ cm$, $h = 10.86\ cm$ and $h = 7.43\ cm$). In addition, the effect of the bottom boundary layer in the inner surf zone is limited to a very narrow region near the bottom, despite the enhanced roughness produced by the sand particles glued to the bottom in those experiments.

7.4 *Evaluation of the radiation stress.*

The wave radiation stress is defined as

$$S_{xx} = \overline{\int_{-h}^{\zeta} (\rho u_w^2 + p_D)\, dz} + \frac{1}{2}\rho g \overline{(\zeta - \overline{\zeta})^2}, \tag{57}$$

where, again the $\overline{()}$ represents wave averaged quantities, u_w is the velocity component due to the wave only, p_D is the dynamic pressure. To the lowest order of approximation retained, $p_D \simeq -\rho w^2$ where w is the vertical velocity. Madsen *et al.* (1997a) calculated the radiation stress from their weakly nonlinear Boussinesq equations, using the approximate expression

$$S_{xx,M} = \rho \frac{Q^2}{h + \zeta} + \frac{1}{2}\rho g \overline{\zeta^2} \tag{58}$$

For weakly nonlinear, weakly dispersive Boussinesq this expression is equivalent to (57), except that the contribution from $\overline{\zeta}^2$ term is neglected.

We define the non-dimensional radiation stress as

$$P \equiv \frac{S_{xx}}{\rho g H^2} = \frac{1}{gH^2} \overline{\int_{-h}^{\zeta} (u_w^2 + p_D)\, dz} + \frac{1}{2} \frac{\overline{(\zeta - \overline{\zeta})^2}}{H^2}. \tag{59}$$

Utilizing the decomposition of the velocity described in the previous subsection, and the fact that below the trough level, the average velocity in the oscillatory

part of the motion is zero, the total wave averaged momentum flux M_{xx} can be expressed as

$$M_{xx} = S_{xx} + \rho \overline{\int_{-h}^{\zeta} (V^2 + 2u_w V)\ dz} \tag{60}$$

which shows that, with S_{xx} defined by (57), the contribution from the current to the total momentum is given by the integral. In the surf zone, it is of further interest to divide S_{xx} into a potential part $S_{xx,p}$ and a breaking part $S_{xx,b}$, writing M_{xx} as

$$M_{xx} = S_{xx,p} + S_{xx,b} + \rho \overline{\int_{-h}^{\zeta} (V^2 + 2u_w V)\ dz} \tag{61}$$

In terms of the dimensionless parameter P $(= P_p + P_b)$, this becomes

$$\frac{M_{xx}}{\rho g H^2} = P_p + P_b + \frac{1}{gH^2} \overline{\int_{-h}^{\zeta} (V^2 + 2u_w V)\ dz} \tag{62}$$

Notice that in the expression (58), Madsen *et al.* (1997a) takes Q as the total volume flux (including the contribution from the net current) which corresponds to defining the radiation stress as

$$S_{xx,M} = S_{xx,p} + \rho \overline{\int_{-h}^{\zeta} (V^2 + 2u_w V)\ dz} \tag{63}$$

Figure 10 shows the cross-shore variation of the radiation stresses, obtained using the model results, for the three wave conditions in Hansen and Svendsen (1979) and also the wave condition given in (Cox *et al.* 1995). The figure shows the total radiation stress as defined by (59) (———), the component of the radiation stress due to the non-breaking part P_p (– – –) and the radiation stress as defined by (58) (– · – · –). Linear theory predicts a constant value of $P = 0.1875$ whereas the maximum obtained from the model is slightly larger than this value. Over most of the domain, the value of P is significantly less than that obtained using linear theory. As the waves shoal, the crests become more and more peaked resulting in decreasing values of P, which has its lowest value just before breaking. Once the waves start breaking, they become more triangular shaped, which results in increasing values of P. Though differing in the details this variation is in qualitative agreement with the results found by Svendsen and Putrevu (1993) from analysis of experimental data.

We also notice that in the cross-shore variation of P which is expected to decrease monotonically towards the breaking point, there is an oscillatory component. The wave period of this oscillation is exactly one half the wave period of the actual wave condition at the boundary. Closer inspection shows that this is because as the waves shoal, they start deviating from the permanent form solution to the Boussinesq equation for that particular water depth. As a result, energy is transferred between the primary and the higher harmonics, in particular between the primary and the second harmonic components, which causes the wavy feature seen in figure 10. Such a feature does not appear for the case of a horizontal bottom.

Direct comparison of $S_x x$ with experimental data is not possible because no measurements are available for the velocity field in the roller region. However, a good assessment of the accuracy of the computed values for $S_x x$ is obtained from the comparisons of the setup shown in part b of the figures 4. 5, and 6, because the setup gradient is essentially equal to the radiations stress gradient. These figures show that, in particular inside the surf zone, the setup is predicted with great accuracy.

8. Conclusions.

A model has been developed for breaking waves which includes the development of vorticity due to the breaking process. The model can therefore also describe the velocity field, due to the short wave motion, in the surf zone, which has not been possible for earlier breaking models. This allows us to predict the horizontal and vertical velocity field in the nearshore region with good accuracy. Therefore, it is possible to obtain not only the wave heights and set-up, but also the wave-averaged quantities such as the mass flux due to the waves, the undertow profiles and the wave radiation stress.

The model is based on the traditional Boussinesq assumptions of long waves with weak non-linearity, which implies that the model is less accurate as the waves approach breaking. On the other hand, comparisons with measured data show that this deficiency is limited to a narrow region starting from just offshore of the breaking

point to just inside of the breaking region. In the surf-zone, from shortly shoreward of the breaking point, the model results agree well with the experimental data, both in prediction of wave heights and in the prediction of the set up.

Comparison with data for the horizontal velocities and the undertow show very excellent agreement. Furthermore, the radiation stress calculated from the model is in qualitative agreement with the results obtained by previous researchers.

Acknowledgments.

This study was sponsored by the National Science Foundation under the grant OCE-9203277 and by the Office of Naval Research under contract No. 98PRO5167-00. The United States Government is authorized to produce and distribute reprints for government purposes notwithstanding any copyright notation that may appear herein.

A. Generation of permanent form waves.

At the offshore boundary, the depth is assumed constant so the Boussinesq equations are, in dimensional form,

$$\zeta_t + Q_x = 0, \tag{A.1}$$

$$Q_t + \left(\frac{Q^2}{h}\right)_x + g(h+\zeta)\zeta_x - \left(B + \frac{1}{3}\right) h^2 Q_{xxt} - Bgh^3\zeta_{xxx} = 0. \tag{A.2}$$

To develop constant form solutions for these equations, we assume that ζ and Q can be expressed in terms of Fourier series

$$\zeta = \sum_{n=1}^{M} \frac{a_n}{2} e^{in\theta} + c.c, \tag{A.3}$$

$$Q = \sum_{n=1}^{M} \frac{b_n}{2} e^{in\theta} + c.c, \tag{A.4}$$

where $\theta = kx - \omega t$ with k the wave number and ω the frequency. Substituting (A.3) and (A.4) into (A.1) and (A.2) gives

$$-\omega a_n + k b_n = 0 \tag{A.5}$$

and

$$-\omega b_n + \frac{k}{2h}\sum_{l=1}^{n-1}\left(b_l b_{n-l} + gh\frac{a_l a_{n-l}}{2}\right) + \frac{k}{h}\sum_{l=n+1}^{M}\left(b_l b_{l-n} + gh\frac{a_l a_{l-n}}{2}\right)$$
$$+ ghka_n - \left(B + \frac{1}{3}\right) h^2 n^2 k^2 \omega b_n + Bgn^2 h^3 k^3 a_n = 0 \tag{A.6}$$

respectively for each $n = 1, 2, ..., M$. In addition, the wave height, defined as $H = \zeta_{max} - \zeta_{min}$ gives

$$H = 2\left(a_1 + a_3 + ...a_N\right), \tag{A.7}$$

where $N = M$ if M is odd and $N = M - 1$ if M is even. (A.5)-(A.7) is a set of $2M + 1$ equations for the $2M + 1$ unknowns a_n, b_n and k, which is solved using the Newton-Raphson iteration method (Press *et al.* 1992).

Note that for a given wave height, wave period and water depth, the solution procedure involves finding not only the Fourier amplitudes a_n and b_n of the water surface elevation and the velocity, but also the wave number k. Thus, the solution implicitly incorporates the solution to the dispersion relation.

B. The absorbing-generating boundary condition.

The absorbing-generating boundary condition used here follows the work of Van Dongeren and Svendsen (1997) which was developed for equations of continuity and momentum locally dominated by the terms corresponding to the non-linear shallow water equations. In our case, this criteria is satisfied since the dispersive terms are considered small. The dimensional equations for a horizontal bottom with no wave breaking can be written as

$$\frac{\partial \zeta}{\partial t} + \frac{\partial Q}{\partial x} = 0, \tag{B.1}$$

$$\frac{\partial Q}{\partial t} + g(h+\zeta)\frac{\partial \zeta}{\partial x} + \left(\frac{Q^2}{h+\zeta}\right)_x = \left(B + \frac{1}{3}\right) h^2 \left(Q\right)_{xxt} + Bgh^3\zeta_{xxx}. \tag{B.2}$$

If we define the variables $d = h + \zeta$, $U = Q/d$ and $\mathcal{G} = \left(B + 1/3\right) h^2 \left(Q\right)_{xxt} + Bgh^3\zeta_{xxx}$, (B.1) and (B.2) can be expressed in matrix form as

$$\frac{\partial \boldsymbol{f}}{\partial t} + \boldsymbol{A}\frac{\partial \boldsymbol{f}}{\partial x} = \boldsymbol{G}, \tag{B.3}$$

where

$$\boldsymbol{f} = \begin{bmatrix} d \\ U \end{bmatrix}, \qquad \boldsymbol{A} = \begin{bmatrix} U & g \\ d & U \end{bmatrix} \qquad \text{and} \qquad \boldsymbol{G} = \begin{bmatrix} 0 \\ \mathcal{G}/d \end{bmatrix} \tag{B.4}$$

The eigenvalues of $\boldsymbol{A}$ are $U \pm \sqrt{gh}$ which are always real. Therefore, a modal matrix $\boldsymbol{P}$ can be constructed from the eigenvectors such that $\boldsymbol{P}^{-1}\boldsymbol{A}\boldsymbol{P}$ is diagonal,

$$\boldsymbol{P} = \begin{bmatrix} \sqrt{h/g} & -\sqrt{h/g} \\ 1 & 1 \end{bmatrix} \quad \text{and} \quad \boldsymbol{P}^{-1} = \frac{1}{2}\begin{bmatrix} \sqrt{g/h} & 1 \\ -\sqrt{g/h} & 1 \end{bmatrix} \tag{B.5}$$

Equation (B.3), can then be re-expressed as

$$\boldsymbol{P}^{-1}\frac{\partial \boldsymbol{f}}{\partial t} + \boldsymbol{P}^{-1}\boldsymbol{A}\boldsymbol{P}\boldsymbol{P}^{-1}\frac{\partial \boldsymbol{f}}{\partial x} = \boldsymbol{P}^{-1}\boldsymbol{G} \tag{B.6}$$

which yields a set of two equations in terms of Q and ζ,

$$\frac{\partial \beta^+}{\partial t} + \left(\frac{Q}{h+\zeta} + \sqrt{g(h+\zeta)}\right)\frac{\partial \beta^+}{\partial x} = \mathcal{G}/(h+\zeta), \tag{B.7}$$

$$\frac{\partial \beta^-}{\partial t} + \left(\frac{Q}{h+\zeta} - \sqrt{g(h+\zeta)}\right)\frac{\partial \beta^-}{\partial x} = \mathcal{G}/(h+\zeta). \tag{B.8}$$

with

$$\beta^+ = U + 2\sqrt{gh}, \tag{B.9}$$

$$\beta^- = U - 2\sqrt{gh} \tag{B.10}$$

Here β^+ is the incoming characteristic and β^- is the outgoing characteristic. For our purpose, it is the outgoing characteristic which gives the information about the waves which are propagating away from the shoreline. We now have to assume something about the interaction between the incoming waves, which are specified and the outgoing waves which are unknown. Both the volume flux and surface elevation can be divided into an incoming and outgoing component

$$Q = Q_i + Q_r \qquad \text{and} \qquad \zeta = \zeta_i + \zeta_r,$$

where the subscript i denotes quantities coming into the domain and the subscript r represents the outgoing components.

Following Van Dongeren and Svendsen (1997), we utilize that the linear terms in the equations are $O(1)$ and the $O(\delta, \mu^2)$ terms are considered small. Thus, the expression for β^- is, keeping terms up to $O(\delta^2)$

$$\begin{aligned}\beta^- &= U_i + U_r - 2\sqrt{gh\left(1 + \frac{\zeta_i + \zeta_r}{h}\right)} \\ &= U_i + U_r - 2\sqrt{gh}\left(1 + \frac{\zeta_i + \zeta_r}{2h} - \frac{(\zeta_i + \zeta_r)^2}{8h}\right) + O\left(\delta^3\right).\end{aligned} \tag{B.11}$$

We now express the water surface elevations (ζ_i and ζ_r) in terms of the velocities (U_i and U_r) utilizing the relation

$$U_i = \frac{c\zeta_i}{h + \zeta_i}, \qquad U_r = -\frac{c\zeta_r}{h + \zeta_r}, \qquad c = \sqrt{g(h + \zeta_i + \zeta_r)}. \tag{B.12}$$

After some algebraic manipulations, the water surface elevations ζ_i and ζ_r can be expressed in terms of the velocities as

$$\frac{\zeta_i}{h} = \frac{U_i}{c_0} + \frac{1}{2}\frac{U_i^2}{c_0^2} + \frac{U_i U_r}{2c_0^2} + O\left(\frac{\zeta_i^3}{h^3}\right), \tag{B.13}$$

$$\frac{\zeta_r}{h} = -\frac{U_r}{c_0} + \frac{1}{2}\frac{U_r^2}{c_0^2} + \frac{U_i U_r}{2c_0^2} + O\left(\frac{\zeta_r^3}{h^3}\right), \tag{B.14}$$

where $c_0 = \sqrt{gh}$ and both ζ_i/h, $\zeta_r/h \simeq O(\delta)$. Substituting (B.13) and (B.14) into (B.11) gives

$$\frac{\beta^-}{c_0} = -2 - \frac{1}{4}\frac{U_i^2}{c_0^2} - \frac{3}{2}\frac{U_i U_r}{c_0^2} + 2\frac{U_r}{c_0} - \frac{1}{4}\frac{U_r^2}{c_0^2}. \tag{B.15}$$

Solving this equation with respect to U_r, the outgoing component is calculated as

$$\frac{U_r}{c_0} = \left(-3\frac{U_i}{c_0} + 4\right) \pm 2\sqrt{2\frac{U_i^2}{c_0^2} - 6\frac{U_i}{c_0} + 4 - \left(\frac{\beta^-}{c_0} + 2\right)}. \tag{B.16}$$

The still water condition is

$$U_r = 0, \qquad U_i = 0 \qquad \text{and} \qquad \frac{\beta^-}{c_0} + 2 = 0, \tag{B.17}$$

which gives the positive root as the spurious root, which leaves

$$\frac{U_r}{c_0} = \left(-3\frac{U_i}{c_0} + 4\right) - 2\sqrt{2\frac{U_i^2}{c_0^2} - 6\frac{U_i}{c_0} - \left(\frac{\beta^-}{c_0} - 2\right)}. \tag{B.18}$$

During the solution of the Boussinesq equations the values of Q and ζ are calculated at the next time step at all interior points of the computational domain. The expression (B.18) makes it possible also to upgrade Q_r and hence Q at the boundary points to the next time step. For further details about the derivations see Van Dongeren and Svendsen (1997).

Figure 11 shows the performance of the boundary condition for two sample input wave conditions. For both cases, the initial condition is no waves in the domain ($\zeta = 0$ everywhere in the domain). Waves are generated at the boundary during $t = 0 - 6T$. The waves are tapered with a hyperbolic tangent function to suppress transients during the first and last period. The waves propagate up to a wall where they are reflected. The reflected waves then pass through the absorbing-generating boundary at $x = 0$. The length of the wave tank (λ) was 5.0 m for the first case and 20 m for the second.

Figure 11(a) shows the time series at the absorbing-generating boundary at $x = 0$ for a long wave of $T\sqrt{g/h} = 26$ and $L/\lambda \simeq 2$, where L is the wave length. The waves reflected from the wall boundary reaches the absorbing-generating boundary

while waves are still being generated and sent into the domain. As a result, standing waves are present in the domain for most of time the waves are in domain. Due to the dispersive nature of the equations, there is a tail of very short waves for the reflected waves. These small waves propagate slowly out of the domain. It is seen that still water condition is recovered quickly. Figure 11(b) shows the time series at $x = 0$ for a much shorter wave of $T\sqrt{g/h} = 10.5$ and with $L/\lambda \simeq 0.2$. The recovery of still water conditions takes a longer time in this case, probably also as a result of the length of the domain in comparison to the wave length. Overall, the performance of this boundary condition is very good for regular waves.

References

Bakunin, J. (1995). Experimental study of hydraulic jumps in low Froude number range. Master's thesis, Center for Applied Coastal Research, University of Delaware, Newark, DE19716.

Boussinesq, J. (1872). Theorie des ondes et des remous qui se propagent le long d'un canal rectangulaire horizontal. *en communiquant au liquide contenu dans ce canal des vitesses sensiblement pareilles de la surface au fond. Journal Math. Pures et Appl. 2nd series 17*, pp. 55–108.

Brocchini, M., P. Cherubini, and L. Iovenitti (1991). An extension of Boussinesq type model to the surf zone. *Computer modelling in ocean engineering 91*, Rotterdam, The Netherlands, pp. 349–359.

Cox, D. T., N. Kobayashi, and A. Okayasu (1995). Experimental and numerical modeling of surf zone hydrodynamics. Technical Report CACR-95-07, Center for Applied Coastal Research, University of Delaware.

Deigaard, R. and J. Fredsoe (1989). Shear stress distribution in dissipative water waves. *Coastal Engng. 13*, pp. 357–378.

Dingemans, M. W. (1997). *Water wave propagation over uneven bottoms. Part 2 - Nonlinear wave propagation*, Volume 13 of *Advanced series on Ocean Engng.* World Scientific.

Gobbi, M. F., J. T. Kirby, and G. Wei (1999). A fully nonlinear Boussinesq model for surface waves. II. Extension to $O(kh)^4$. *J. Fluid Mech.*, In press.

Hansen, J. B. and I. A. Svendsen (1979). Regular Waves in Shoaling Water: Experimental Data. Technical report, ISVA Series Paper 21.

Karambas, T. K. and C. Koutitas (1992). A breaking wave propagation model based on the Boussinesq equations. *Coastal Engng. 18*, pp. 1–19.

Lin, J. C. and D. Rockwell (1994). Instantaneous structure of a breaking wave. *Phys. Fluids 6(9)*, pp. 2877–2879.

Lin, P. and P. L. F. Liu (1998a). A numerical study of breaking waves in the surf zone. *J. Fluid Mech. 359*, pp. 239–264.

Lin, P. and P. L. F. Liu (1998b). Turbulence transport, vorticity dynamics, and solute mixing under plunging breaking waves in surf zone. *J. Geophysical Res. 103*, pp. 15677–15694.

Madsen, P. A., B. Banijamali, H. A. Schäffer, and O. R. Sørensen (1996). Boussinesq type equations with high accuracy in dispersion and nonlinearity. *Proc. of 25rd ICCE*, ASCE, pp. 95–108.

Madsen, P. A., R. Murray, and O. R. Sørensen (1991). A new form of Boussinesq equations with improved dispersion characteristics. *Coastal Engng. 15*, pp. 371–388.

Madsen, P. A. and H. A. Schäffer (1998a). Higher order Boussinesq-type equations - derivation and analysis. *Phil. Trans. R. Soc. Lond., Series A, 356*, pp. 3123–3184.

Madsen, P. A. and H. A. Schäffer (1998b). A review of Boussinesq-type equations for gravity waves. P. L.-F. Liu (Ed.), *Advances in Coastal and Ocean Engng.*, Volume 5, pp. 90. World Scientific, Singapore.

Madsen, P. A. and O. R. Sørensen (1993). Bound waves and triad interactions in shallow water. *Ocean Engng. 20*, pp. 359–388.

Madsen, P. A., O. R. Sørensen, and H. A. Schäffer (1997a). Surf zone dynamics simulated by a Boussinesq type model. Part I. Model description and cross-shore motion of regular waves. *Coastal Engng. 32*, pp. 255–287.

Madsen, P. A., O. R. Sørensen, and H. A. Schäffer (1997b). Surf zone dynamics simulated

by a Boussinesq type model. Part II. Surf beat and swash oscillations for wave groups and irregular waves. *Coastal Engng. 32*, pp. 289–319.

Madsen, P. A. and I. A. Svendsen (1983). Turbulent bores and hydraulic jump. *J. Fluid Mech. 129*, pp. 1–25.

Mei, C. C. (1992). *The applied dynamics of ocean surface waves* (2nd ed.). World Scientific.

Mei, C. C. and B. LeMehaute (1966). Note on the equations of long waves over an uneven bottom. *J. Geophysical Res. 71*(2), pp. 393–400.

Nwogu, O. (1993). An alternative form of the Boussinesq equations for nearshore wave propagation. *ASCE J. Waterway, Port, Coastal and Ocean Engng. 119*, pp. 618–638.

Peregrine, D. H. (1967). Long waves on beaches. *J. Fluid Mech. 27*, pp. 815–827.

Press, W. H., B. P. Flannery, S. A. Teukolsky, and W. T. Vetterling (1992). *Numerical recipes in fortran* (2nd ed.). Cambridge: University Press.

Schäffer, H. A., P. A. Madsen, and R. Deigaard (1993). A Boussinesq model for wave breaking in shallow water. *Coastal Engng. 20*, pp. 185–202.

Svendsen, I. A. (1984a). Mass flux and undertow in a surf-zone. *Coastal Engng. 8*, pp. 347–365.

Svendsen, I. A. (1984b). Wave heights and set-up in a surf-zone. *Coastal Engng. 8*, pp. 303–329.

Svendsen, I. A. and U. Putrevu (1993). Surfzone wave parameters from experimental data. *Coastal Engng. 19*, pp. 283–310.

Svendsen, I. A., J. Veeramony, J. Bakunin, and J. T. Kirby (1999). The flow in weak turbulent hydraulic jumps. Submitted to *J. Fluid Mech.*

Svendsen, I. A., K. Yu, and J. Veeramony (1996). A Boussinesq breaking wave model with vorticity. *Proc. of 25rd ICCE*, ASCE, pp. 1192–1204.

Van Dongeren, A. R. and I. A. Svendsen (1997). Absorbing-Generating boundary condition for shallow water models. *ASCE J. Waterway, Port, Coastal and Ocean Engng. 123*(6), pp. 303–313.

Wei, G. and J. T. Kirby (1995). A time dependent numerical code for extended Boussinesq equations. *ASCE J. Waterway, Port, Coastal and Ocean Engng. 120*, pp. 251–261.

Wei, G., J. T. Kirby, S. T. Grilli, and R. Subramanya (1995). A fully nonlinear Boussinesq model for surface waves. I. Highly nonlinear, unsteady waves. *J. Fluid Mech. 294*, pp. 71–92.

Zelt, J. A. (1991). The run-up of nonbreaking and breaking solitary waves. *Coastal Engng. 15*, pp. 205–246.

Case No.	$T\ (s)$	$H\ (cm)$	$T\sqrt{g/h}$
1	3.3333	4.3	17.4
2	2.5	3.9	13.0
3	2.0	3.6	10.44

Table 1: Wave parameters from Hansen and Svendsen (1979) at the toe of the beach.

Line No.	L1	L2	L3	L4	L5	L6
h (cm)	28.0	21.14	17.71	14.29	10.86	7.43

Table 2: Location of measuring lines for the data of Cox *et al.* (1995)

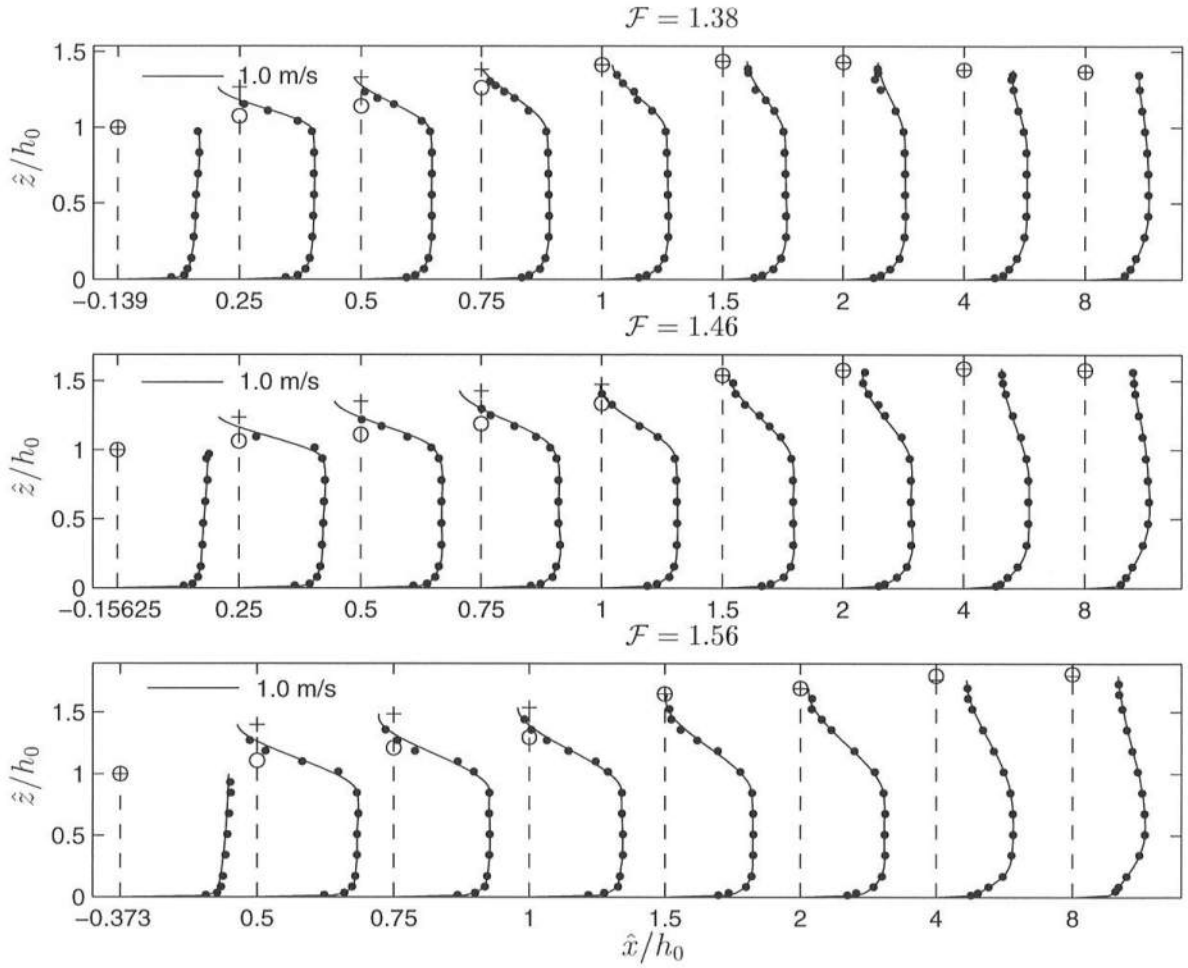

Figure 1: Measured horizontal velocities (•) and curve fits to the velocity (———), the mean water surface (+) and the calculated location of the dividing streamline (○) for all three jumps (from Svendsen *et al.* 1999). h_0 is the depth at the upstream measurement location.

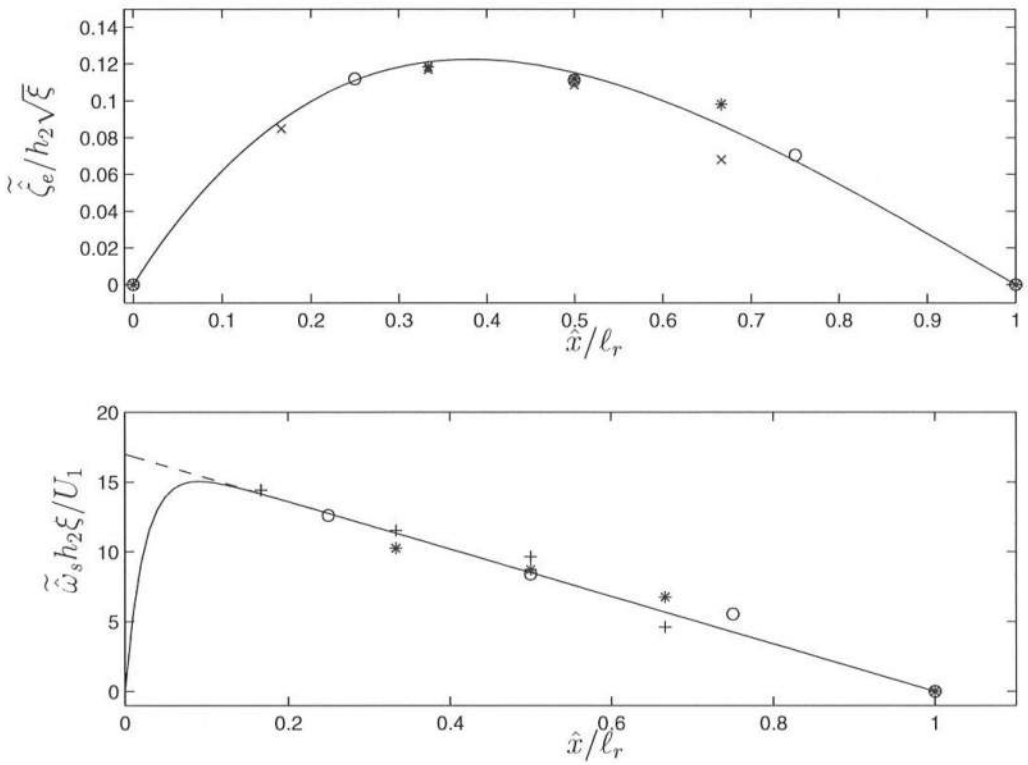

Figure 2: (a) The non-dimensional thickness of the roller for the hydraulic jumps: Data for Froude numbers 1.38($\circ$), 1.46($\times$), 1.56($*$) and least-squares fit (———). (b) Non-dimensional vorticity at the lower edge of the roller with least squares linear fit (– – –) and according to (49)(———).

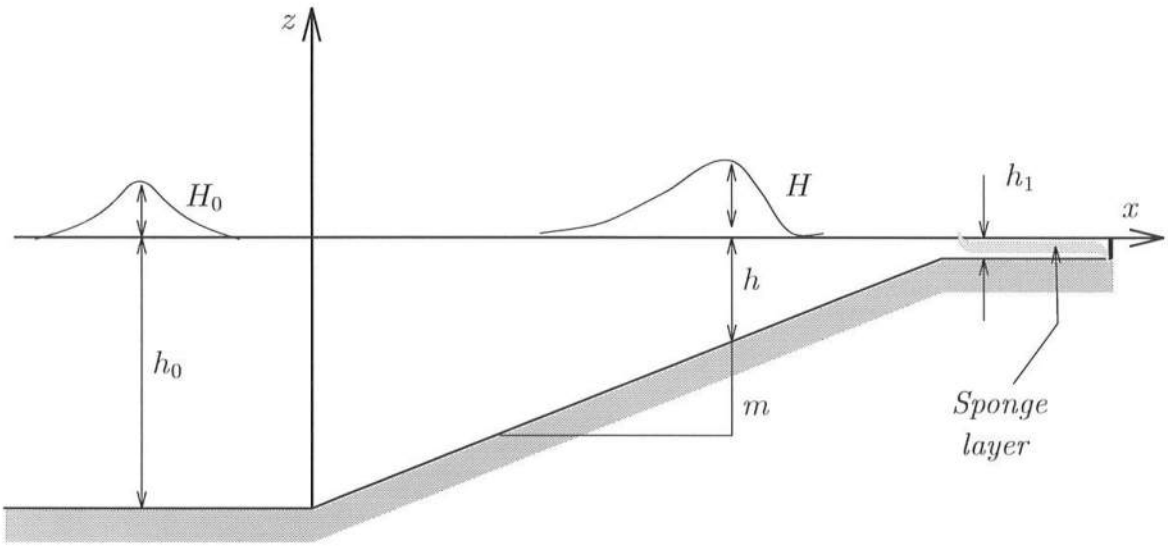

Figure 3: Schematic figure showing the computational domain.

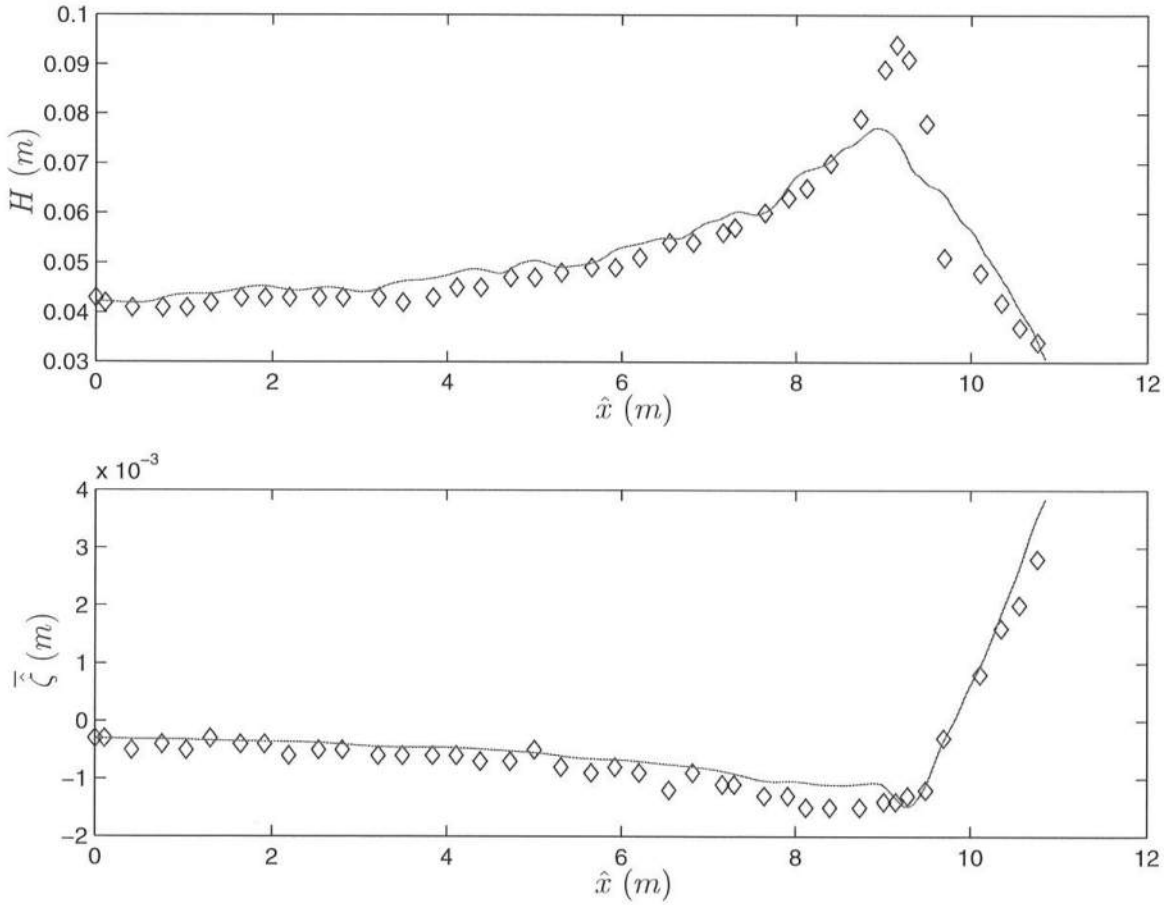

Figure 4: Comparison between model results (———) and data (◇) from Hansen and Svendsen (1979) of wave heights (a) and setup (b) for Case 1 in table 1. The slope starts at $x = 0\,m$.

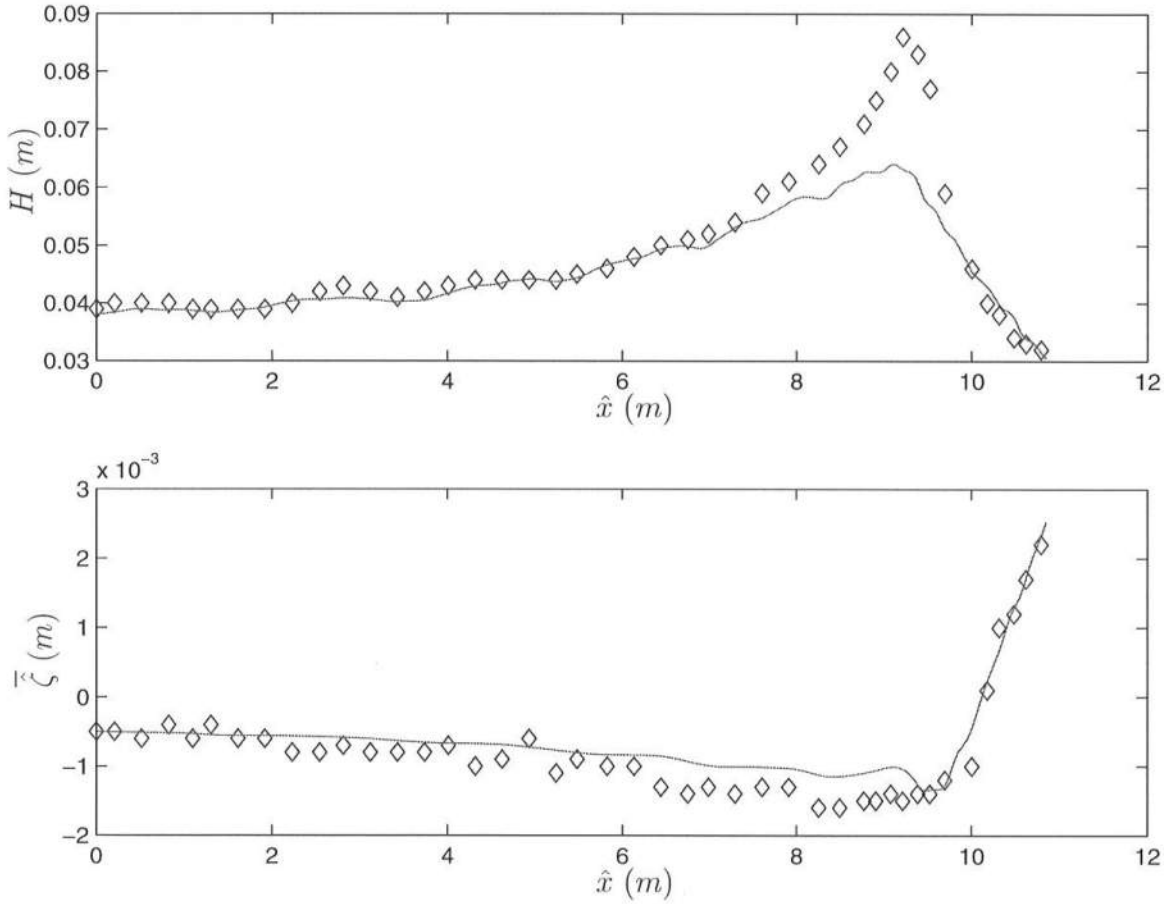

Figure 5: Comparison between model results (———) and data (◇) from Hansen and Svendsen (1979) of wave heights (a) and setup (b) for Case 2 in table 1. The slope starts at $x = 0\,m$.

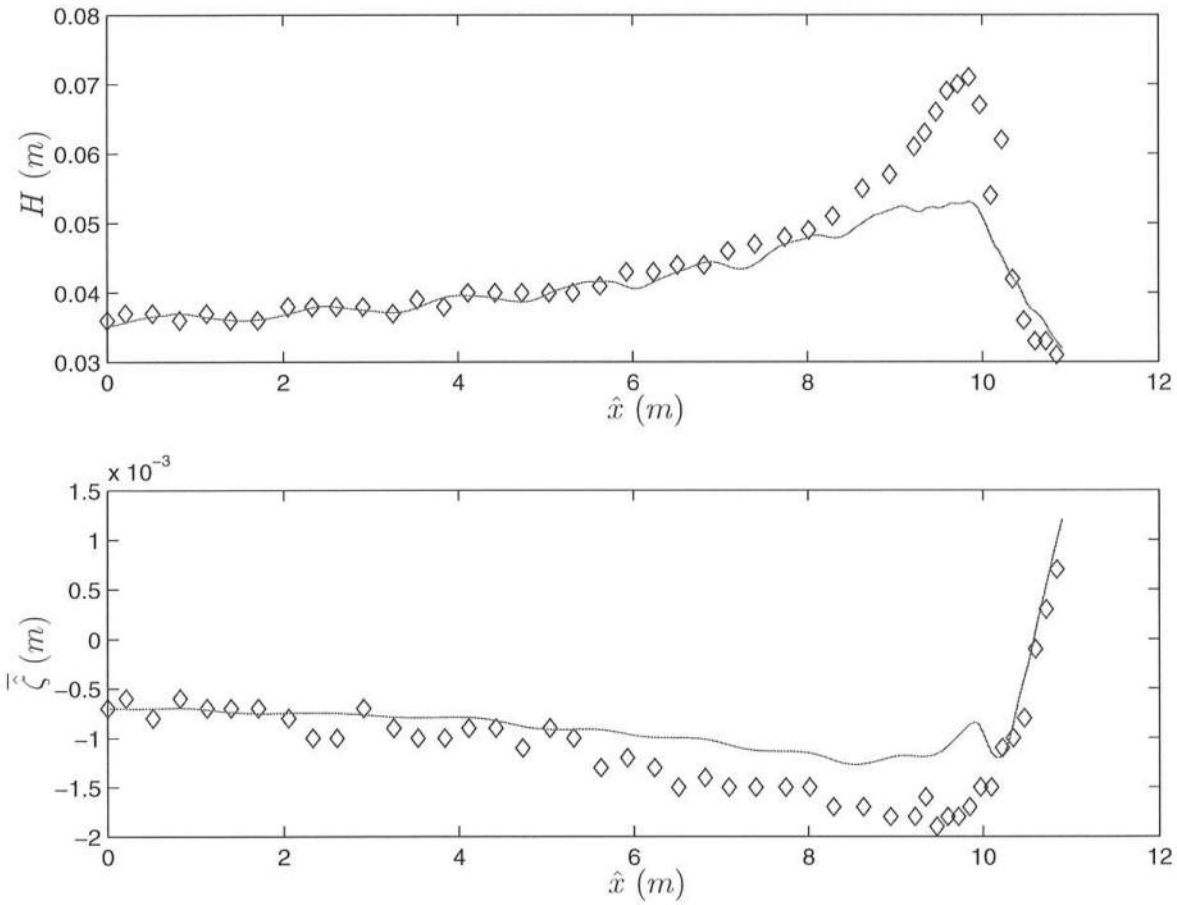

Figure 6: Comparison between model results (———) and data(◇) from Hansen and Svendsen (1979) of wave heights (a) and setup (b) for Case 3 in table 1. The slope starts at $x = 0\,m$.

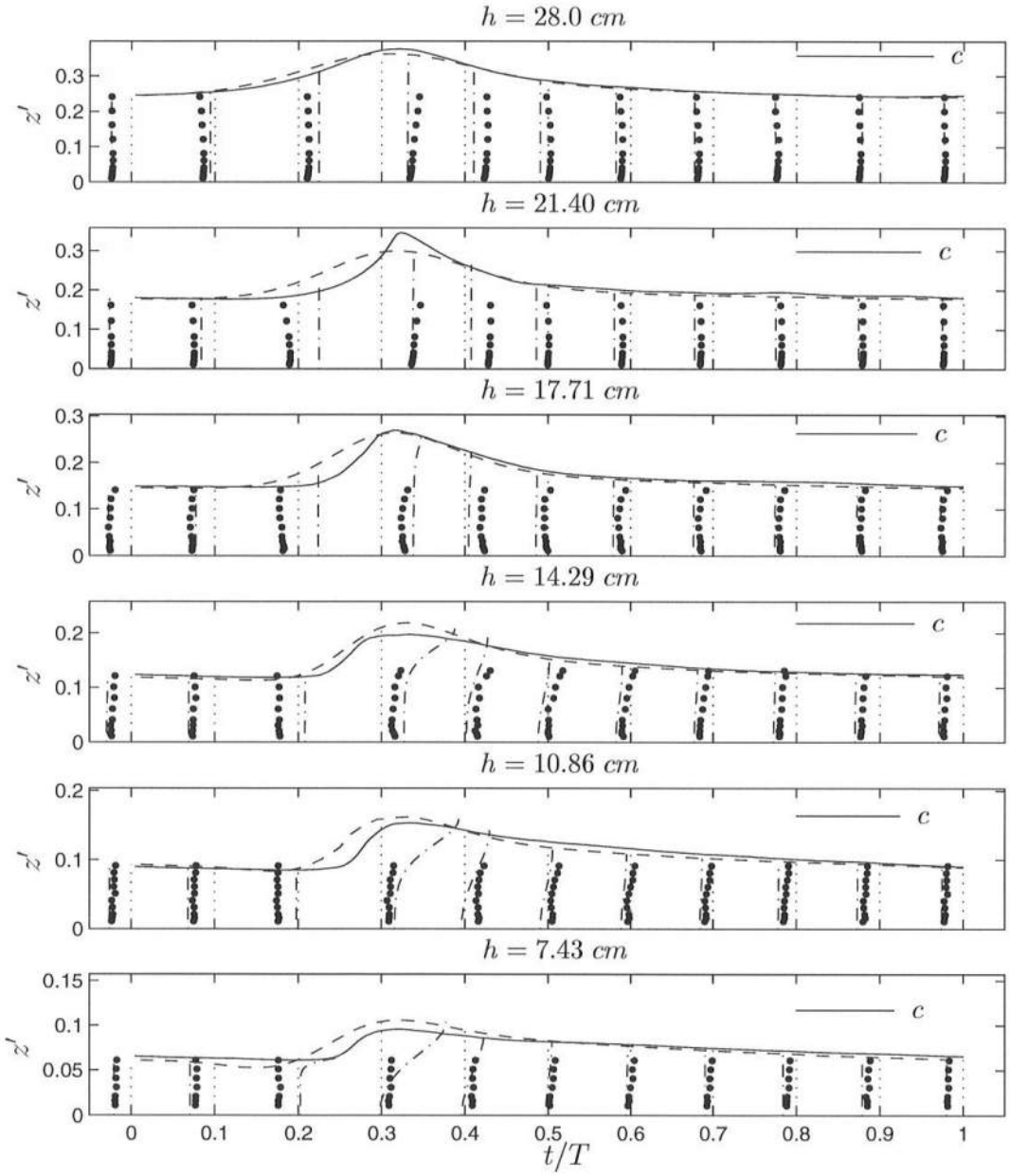

Figure 7: Comparison of velocity profiles between the breaking model (– · – · –) with experimental data from Cox *et al.* (1995) (•) and of water surface elevation (model '– – –', data '———'). The horizontal line at the top right of each sub-plot is the magnitude of the wave speed. The ordinate $z' = z + h$ is zero at the bottom.

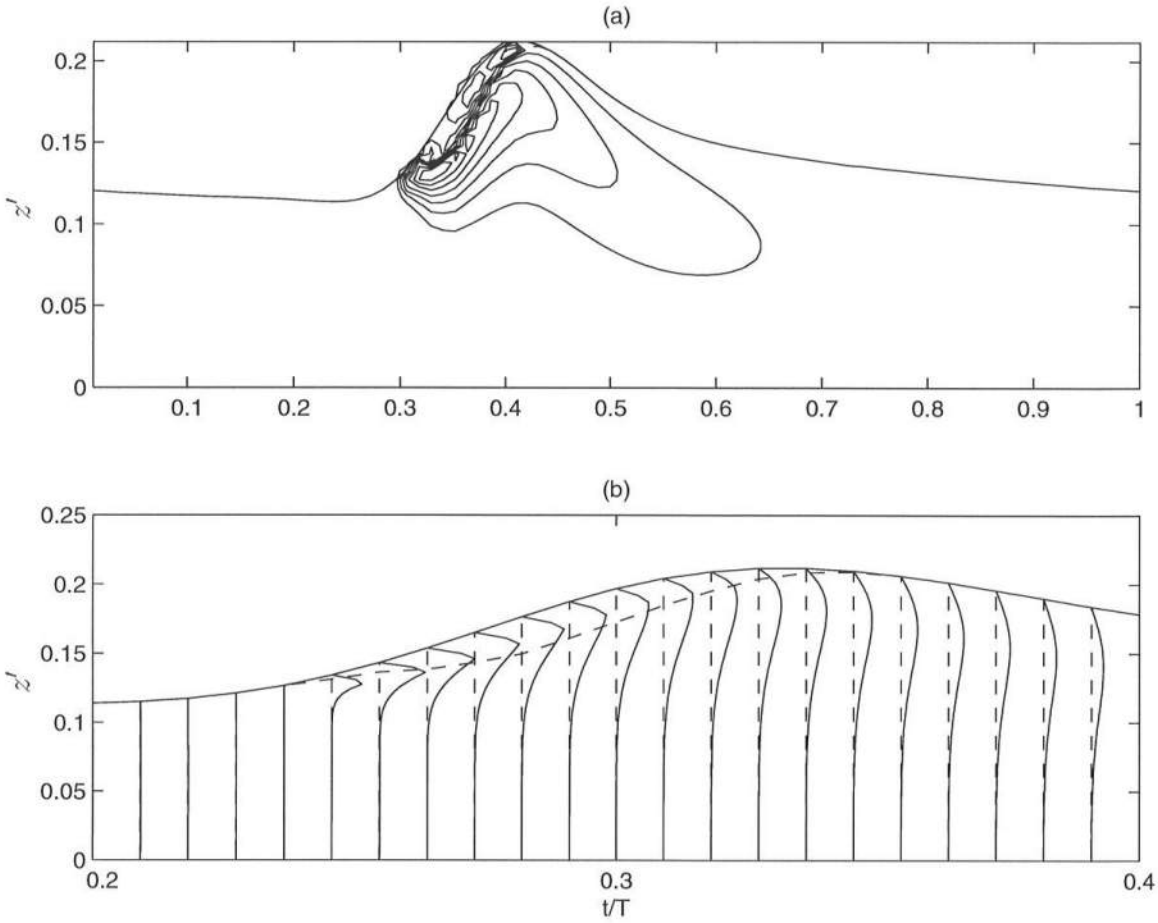

Figure 8: (a) Contours of vorticity at $h = 14.29\ cm$. (b) Vertical profiles of vorticity under the roller and behind the crest at $h = 14.29\ cm$. The ordinate $z' = z + h$ is zero at the bottom.

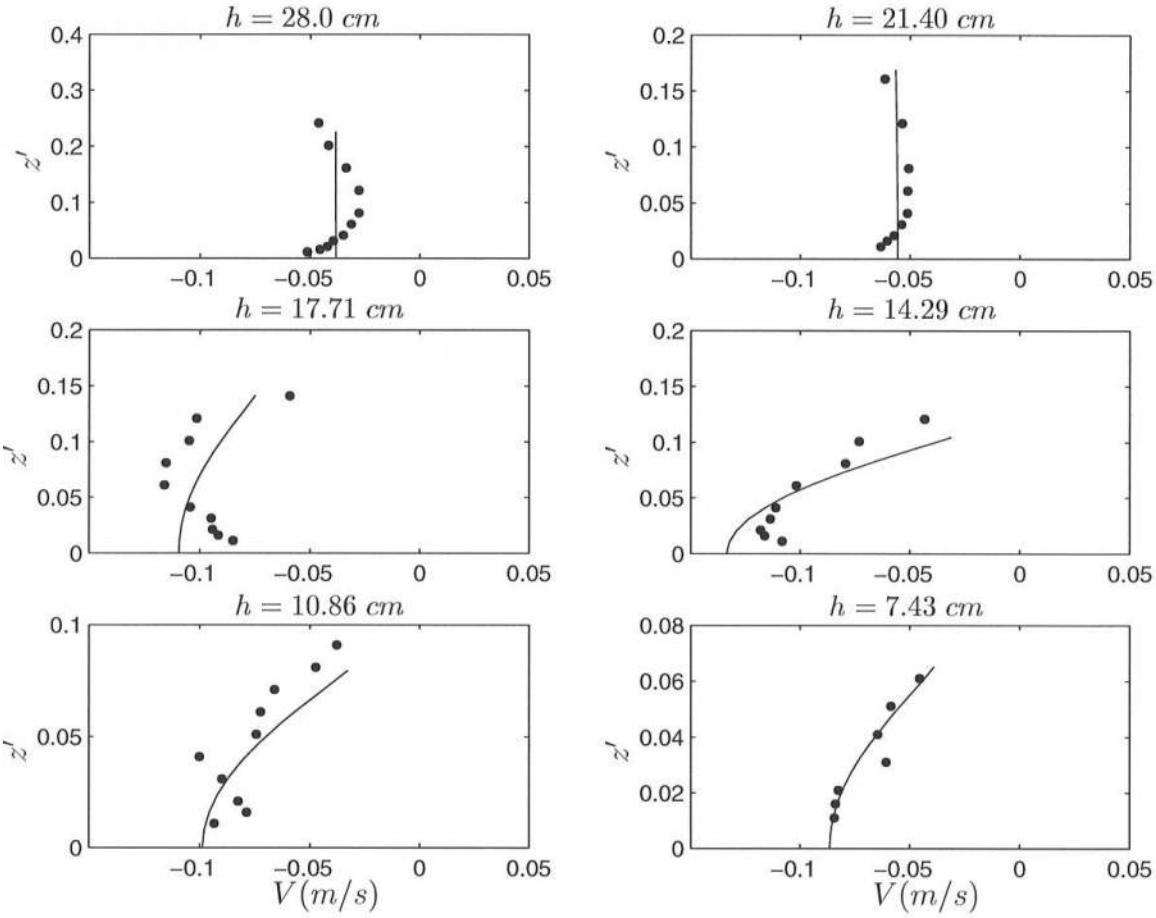

Figure 9: Comparison of the undertow profiles from the model results (———) and the data (•) of Cox *et al.* (1995). The ordinate $z' = z + h$ is zero at the bottom.

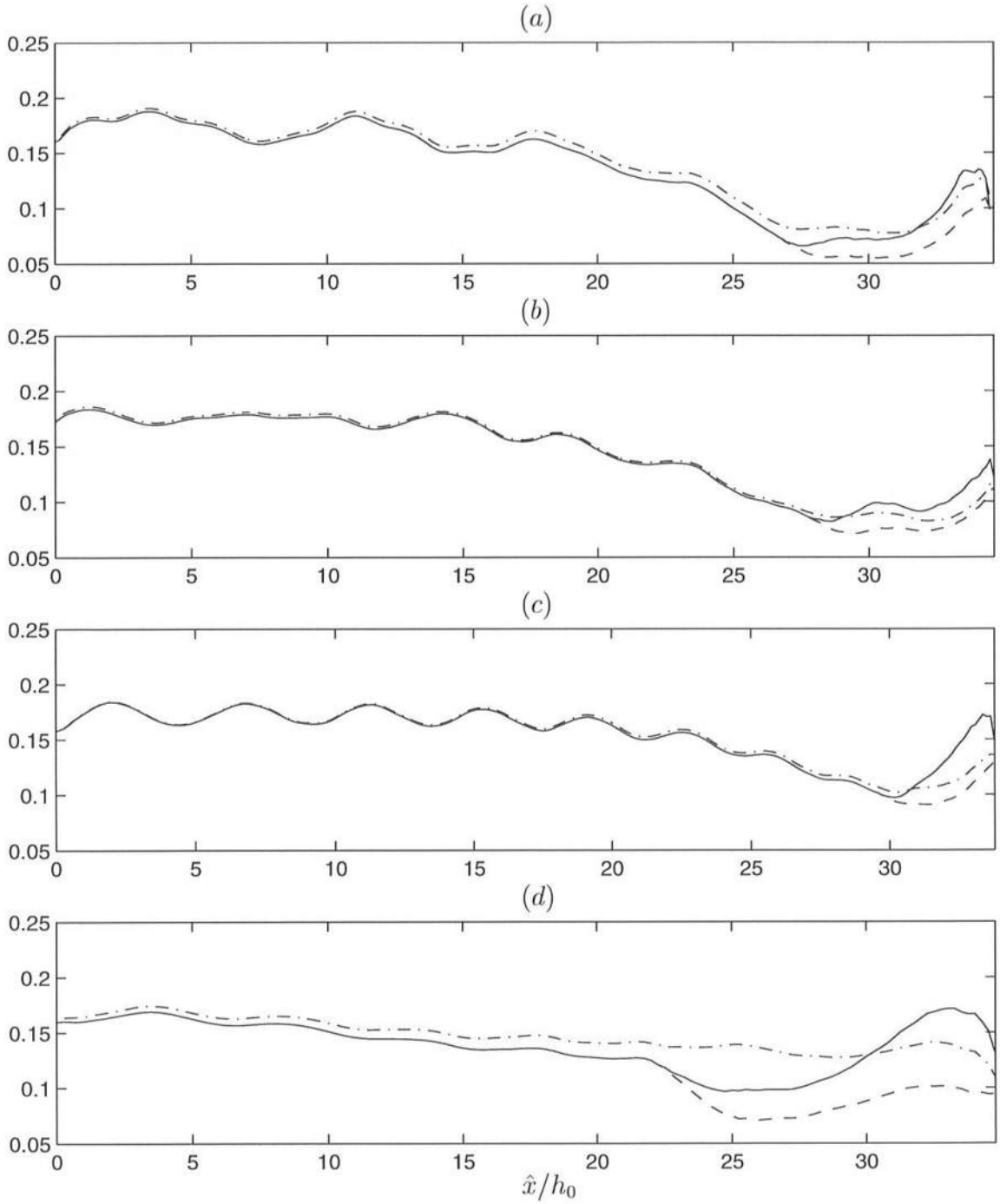

Figure 10: The non-dimensional radiation stress P (———), the potential part P_p (– – –) and using the definition given by Madsen *et al.* (1997a) (–·–·–) for the wave conditions of Hansen and Svendsen (1979) (a) Case 1, Table 1 (b) Case 2, Table 1 (c) Case 3, Table 1 and (d) for Cox *et al.* (1995).

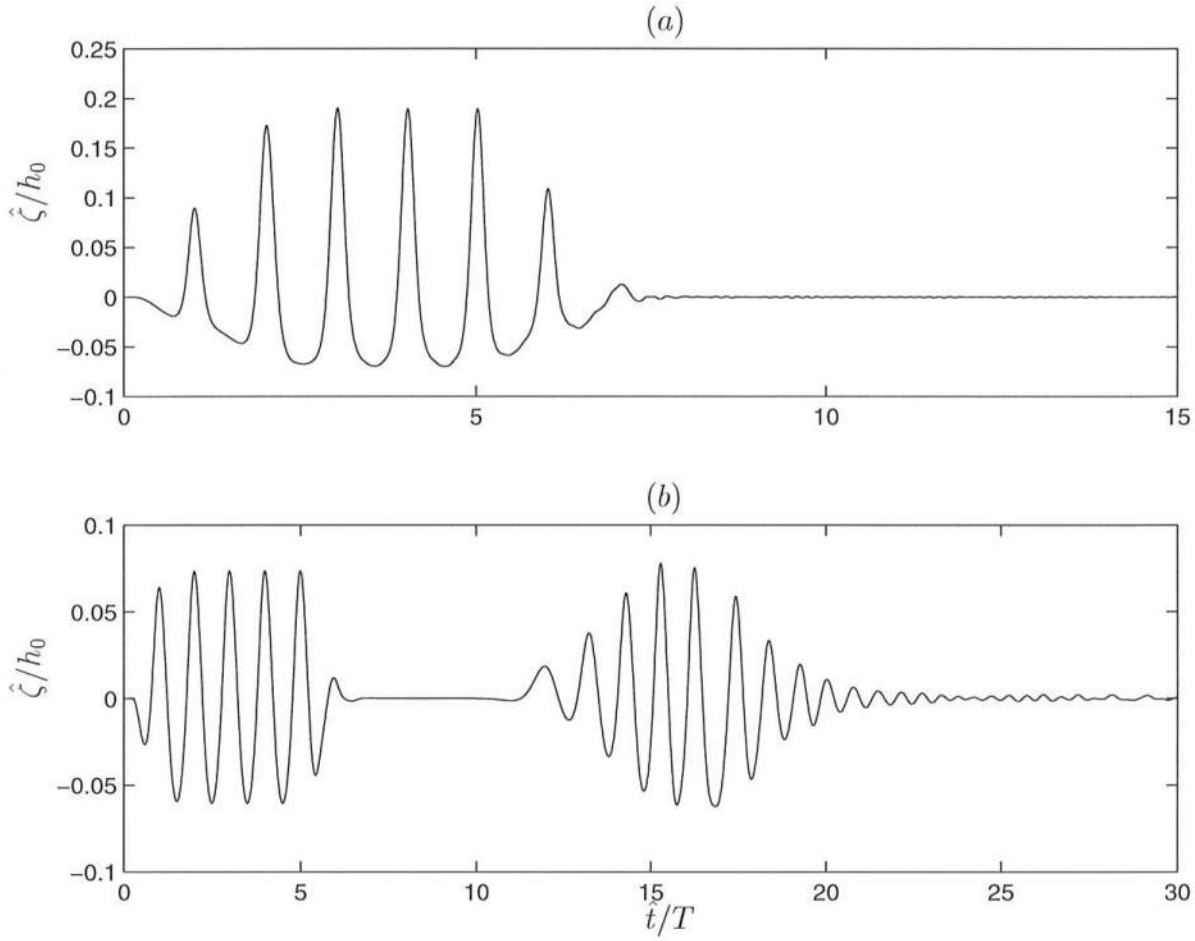

Figure 11: Time series of the water surface elevation at the boundary ($x = 0$) for the fully non-linear model, showing the effect of the absorbing generating boundary condition. (a) long waves ($T\sqrt{g/h} = 26$) (b) short waves ($T\sqrt{g/h} = 10.5$).